PAPER

Preflight radiometric calibration of a carbon dioxide spectrometer

View the article online for updates and enhancements.

Preflight radiometric calibration of a carbon dioxide spectrometer

Shuai Li[1,2], **Chengliang Li**[1,2], **Shuyan Xu**[1], **Hang Zhang**[1] and **Yuquan Zheng**[1,3]

[1] Changchun Institute of Optics, Fine Mechanics and Physics, Chinese Academy of Sciences, Changchun, People's Republic of China
[2] University of Chinese Academy of Sciences, Beijing, People's Republic of China

E-mail: lishuai8028@163.com and zhengyq@sklao.ac.cn

Abstract

The first Chinese Carbon Dioxide Observation Satellite (TanSat), which is designed to make high-precision, high-spatial resolution measurements of carbon dioxide, was successfully launched on 22 December 2016. There are two instruments installed on the TanSat: the High Resolution Hyper-Spectral Sensor for carbon observation Grating Spectrometer, aiming at measuring the amount of carbon dioxide (CO_2) in the atmosphere, and the cloud and aerosol polarimetric imager to identify the disturbance by clouds and to detect the impact of aerosol within the instrument instantaneous field of view. The two instruments work together to make global, high-precision CO_2 measurements with exactly correction of cloud and aerosol interference. The major content of this paper is the laboratory radiometric calibration of ACGS. Both the gain coefficients and the dark current response of each channel were determined during instrument-level ground testing. The gain coefficients for the ACGS were characterized by measuring the instrument response to illumination by an integrating sphere at several light levels. The dark response was calibrated with additional thermal balance testing. This paper also identified bad pixels, recorded in a table of data elements, to be omitted in science data processing. The uncertainties achieved during the radiometric calibration were below 5% ($k = 1$), meeting the absolute calibration mission requirements.

Keywords: remote sensing, radiometric calibration, grating spectrometer, integrating sphere, carbon dioxide

(Some figures may appear in colour only in the online journal)

1. Introduction

The atmospheric concentration of carbon dioxide has been increasing since the age of industrialization, several countries have already launched optical remote sensing monitoring instruments, aimed at studying the global mapping status and change process of concentrations of carbon dioxide over time [1]. The greenhouse gases observing satellite (GOSAT), a Japanese JAXA mission, is designed to monitor greenhouse gases globally using Fourier-Transform spectrometry taking measurements in the thermal and near-infrared bands [2, 3]. The orbiting carbon observatory-2 (OCO-2), a NASA mission, is designed to measure the column-averaged CO_2 dry air mole fraction from space [4, 5].

The GOSAT and OCO-2 have provided a large amount of observational data to infer atmospheric CO_2 concentrations.

As the first Chinese satellite to take space-based measurements of atmospheric CO_2, TanSat is dedicated to characterizing sources and sinks regionally, and quantify the changes over time with precision, coverage and resolution [6]. The instruments onboard the satellite are the High Resolution Hyper-Spectral Sensor for carbon observation Grating Spectrometer (ACGS) and the cloud and aerosol polarimetric imager (CAPI), developed by the Changchun Institute of Optics, Fine Mechanics and Physics, Chinese Academy of Sciences. ACGS is a high spectral and spatial resolution

---

[3] Author to whom any correspondence should be addressed.

Table 1. Spectral performance requirements of ACGS.

Parameter	Band		
	O$_2$A	WCO$_2$	SCO$_2$
Central wavelength/nm	760	1610	2060
Spectral ranges/nm	758–778	1594–1624	2042–2082
Spectral resolutions/nm	0.033–0.047	0.120–0.142	0.160–0.182
Spectral sampling/FWHM	>2	>2	>2

grating spectrometer dedicated to measure the carbon dioxide and oxygen absorption spectra [7]. CAPI is designed to identify the disturbance by clouds and to detect the impact of aerosol within the instrument instantaneous field of view [8]. This paper addresses the prelaunch radiometric calibration of the ACGS performed during thermal vacuum testing and it is organized as following. Section 2 provides a description of the ACGS. Section 3 describes the preflight laboratory calibration methodology, including measurement of the instrument dark response and gain coefficients. Results of preflight radiometric calibration are also given in this section. The bad pixels detection method based on dark background data and radiometric response data is described in section 4, followed by concluding remarks in section 5.

2. Description of the ACGS

As the main payload of TanSat, ACGS is designed to measure total absorption on the way of sunlight propagation the sun—earth surface—satellite in three narrow bands, including the strong CO$_2$ band from 2.042 μm to 2.082 μm, the near infrared weak CO$_2$ band ranging from 1.594 μm to 1.624 μm and the O$_2$A band covering 0.758 μm to 0.778 μm. The spectral resolving power of the O$_2$A band is about 19 000, and the two CO$_2$ bands are about 12 000. The spectral performance requirements are summarized in table 1 [9, 10].

ACGS is designed to measure global atmospheric CO$_2$ concentrations in a Sun-synchronous orbit with an angle of inclination of 98.2°. The local time of the descending node is ~13:30 min and orbital altitude is ~700 km. The three spectral ranges measured by the ACGS instrument observed from space are shown in figure 1, which was taken on January 13, 2017 at Northeastern Indian Peninsula (N21, E96). The spectral range of each channel not only includes the complete molecular absorption spectra, but also some nearby continuum absorbing lines which can provide constraints on the optical properties of aerosols [11]. As the spectra show clear narrow absorption features in all three bands, the instrument can be seen to have low stray light and high signal to noise.

The ACGS instrument consists of three grating spectrometers which are integrated into a common structure with similar optical designs. Figure 2 shows the major optical components and optical path of ACGS, which consists of a specially designed pointing mirror, an afocal telescope, a beam splitter, a focusing system, an entrance slit, a collimating system, a plane

grating and a focal plane imaging system [12]. The pointing mirror, made of aluminum alloy, is mounted on a 1D rotating mechanism. It is specially designed to achieve two functions in double-side: one side works as a mirror to reflect the incident light to the telescope; the other side is a reflecting diffuser intended to perform onboard absolute radiometric calibration of the instrument. The slightly curved entrance slit is used to correct the smile effect and to compensate for optical aberrations of each spectrometer. Once the light enters the slit, it is made accurately parallel by the collimating system, distributed by a plane grating and focused on focal plane array (FPA) with a 2D structure. One dimension measures wavelength variations in the direction perpendicular to slit, and the other records spatial field along the entrance slit.

The O$_2$ A-band deploys the Si detector E2V55-30, which are 1252 × 576 pixel arrays with a pixel pitch of 22.5 μm manufactured by E2V Technologies. The detector operates in a frame transfer mode with excellent anti-blooming, high dynamic range and low dark current. The 1252 × 1152 pixels of detector are split into two sections with 1252 × 576 pixels for each; one is top image area, the other is bottom store area with a store shield. There are 320 pixels out of 576 in spatial dimension parallel to the entrance slit; 5 pixels out of 1252 are blocked out on each side of the array, and the rest 1242 pixels work in the spectral dimension.

The identical mercury cadmium telluride (HgCdTe) detectors are used for the 1.61 μm and 2.06 μm bands respectively, each consists of a 500 × 256 pixels array with a pixel pitch of 30 μm. Each pixel is connected to an input stage to integrate charges and to convert them to an output voltage. The read-out is flexible to allow addressing and reading out any sequence of rows. The eight columns at each edge of each CO$_2$ FPA are masked and returned as unilluminated reference pixels. The Sterling type cryogenic cooler is used to maintain the HgCdTe detectors work at their operating temperature of 150 K.

The active 1242-by-320-pixel region on O$_2$A band FPA and 500-by-240-pixel region on Weak CO$_2$ band and the Strong CO$_2$ band FPA can be read out pixel by pixel, this readout mode is called 'full-frame mode'. This mode is not available for routine scientific imaging due to the restriction of FPA readout time and downlink data volume. Therefore, 'full-frame mode' is only recorded during instrument calibration, and not for routine observations.

The scheme of pixel binning of ACGS is similar to OCO-2, the 320 rows of O$_2$A band and 240 rows of two CO2 band are divided into 9 'footprints', each consisting of 32 and 24 adjacent spatial pixels. The pixels within each footprint are summed by the instrument FPGA processor, so that the active area of the FPAs can be read out in this 'summed mode'. Besides decreasing the readout time and reducing downlink data volume, this onboard summing can also increase spectral sample SNR, especially in low-illumination conditions [13].

3. Laboratory radiometric calibration

A radiometric calibration is needed to obtain high retrieval precision in measuring atmospheric carbon dioxide concentration. The calibration process required the measurement of
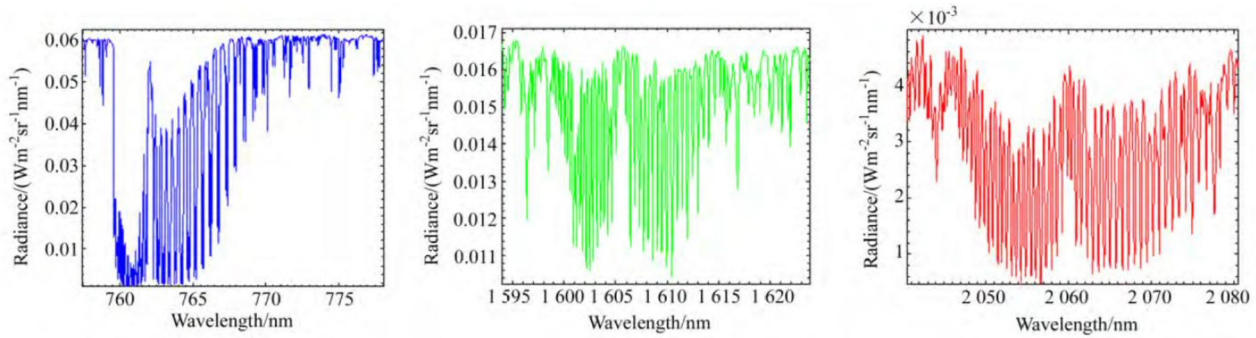
Figure 1. The first atmospheric absorption spectrum collected from ACGS. Data are shown for the O_2 A-Band (left), the Weak CO_2 band (middle) and the Strong CO_2 band (right).
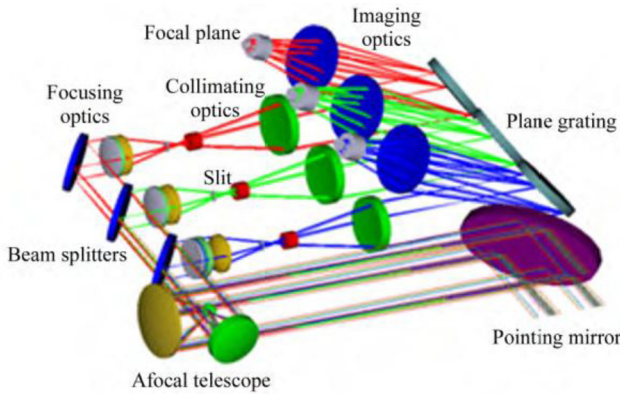

Figure 2. The major optical components and optical path.

the dark current offset, gain and linearity of each instrumental channel. To take accurate measurements of the depth of each absorption line, the standard uncertainty on ACGS was less than 5%, less than 3% for a relative standard uncertainty between bands, and less than 0.1% for the relative standard uncertainty between channels within the same band. This is the same target uncertainty as for the GOSAT and OCO-2 missions [14–18]. Radiometric performance requirements are summarized in table 2. The ACGS instrument was calibrated before it was installed into the spacecraft bus in September to November 2015. In order to calibrate the instrument gain over the entire range of illumination levels expected on orbit, the ACGS was calibrated at more than 30 radiometric levels to cover the full dynamic range. The relationship between an incident radiance and ACGS digital output was established during the radiometric calibration.

3.1. NIST-traceable calibration

The ACGS was calibrated using an integrating sphere as the radiance source, and a FieldSpec 4 Hi-Res analytical spectral device (ASD) was used to transfer the radiance source, the lamp standard, from the integrating sphere to the ACGS. The radiance of the integrating sphere was determined using an ASD that was pre-calibrated in radiance units. The original calibration of the ASD was traceable to NIST. Before the radiometric characterization of the ACGS, the ASD was recalibrated traceable to the NIST through reference radiance source comprising

Table 2. Radiometric performance requirements of ACGS.

Parameter	Band		
	O_2A	WCO_2	SCO_2
Absolute radiometric uncertainty (%)	<5%	<5%	<5%
Relative radiometric uncertainty (%)	<3%	<3%	<3%
Relative error among channels within a band (%)	<0.1%	<0.1%	<0.1%
Dark current error (DNs)	<5 DNs	<5 DNs	<5 DNs
Calibration nonlinearity error (%)	<2%	<2%	<2%

a 1000 W Quartz-Halogen NIST Lamp and a Spectralon diffuser calibrated by Labsphere. A high-precision DC power supply was used to provide a stable current to the lamp, and a high-accuracy digital multimeter and a standard resistor were deployed to measure that current with a precision of 3 mA. This current uncertainty corresponded to a radiance uncertainty of less than 0.05% for the source. A radiance source was obtained by combining the NIST-traceable source with a spectralon diffuser that had been calibrated for its reflectance in 0° and 45° geometry. With the source and diffuser setup for direct incidence, the radiance of the illuminated diffuser was known at 45° and the ASD was calibrated in this geometry. The angle and distance between ASD and the diffuser was fixed, which was determined to ensure that the ASD used a 1° field of view observed the center of the diffuser. The spectral radiance of the diffuser could be calculated as equation (1).

$$L(\lambda) = \frac{E(\lambda)}{\pi}\rho(\lambda). \tag{1}$$

Where $E(\lambda)$ is the spectral irradiance of the standard lamp on the diffuser, $\rho(\lambda)$ is the bidirectional reflectance factor of the diffuser.

The NIST lamp and the Labsphere Spectralon diffuser were placed on the optical rail, whose positioning accuracy was 0.2 mm. A darkroom was built in order to reduce the stray light as much as possible. The black flannel cloth was laid around the test apparatus in the darkroom to shield stray-room light. By sequentially changing the distance between the lamp and the diffuser, the spectral irradiance of the diffuser could be calculated as equation (2).
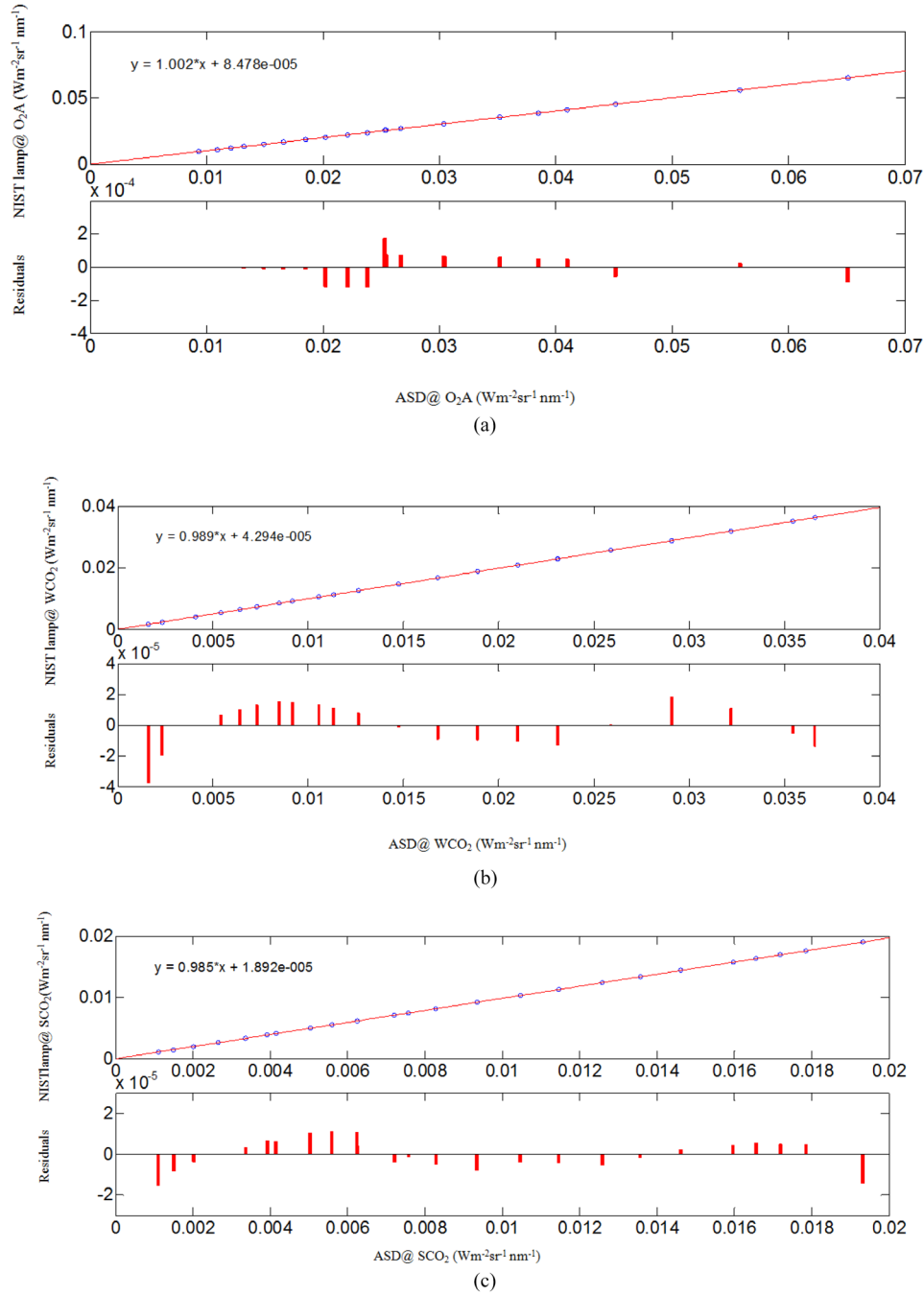
Figure 3. (a) Results of the statistical analysis of the ASD NIST standard traceability of O_2A band. (b) Results of the statistical analysis of the ASD NIST standard traceability of WCO_2 band. (c) Results of the statistical analysis of the ASD NIST standard traceability of SCO_2 band.

$$E(l, \lambda) = E(d, \lambda) \frac{d^2}{l^2}. \qquad (2)$$

Where λ is the wavelength of each band, l is distance between the NIST lamp and the diffuser, d is distance between the NIST lamp and the diffuser provided by the vendor. This lamp was aligned to a reference plane at the filament and no correction for filament offset was used. $E(d, \lambda)$ is the spectral irradiance of the diffuser when the distance between the NIST lamp and the diffuser is d. The maximum and minimum lamp-diffuser distances were 1320 mm and 500 mm in the O_2A band, 2400 mm and 500 mm in the WCO_2 band, and 2100 mm and 500 mm in the SCO_2 band. The 500 mm reference distance

between the NIST lamp and the Labsphere Spectralon diffuser was determined by the block gauge and the distance error was within 1 mm.

The accuracy and stability of the ASD could be determined by statistically analyzing and comparing the spectral radiance between calculated using equation (2) and output of ASD. The correlations between the NIST lamp and the ASD output and the residuals can be seen in figure 3. The agreement between the NIST lamp and the ASD was good, as demonstrated by the small fitting residuals. The ASD calibration against lamp-diffuser source uncertainty was less than 0.3%, which included the distance measurement error and the fitting residuals.
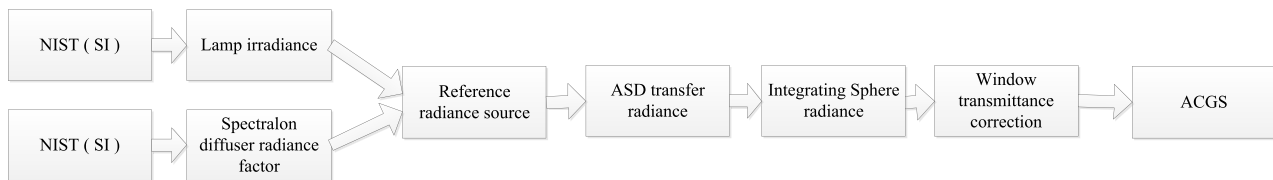
Figure 4. Illustration of standard traceability and ACGS calibration chain.

Thus, the radiance responsivity of the ASD was determined traceably to the NIST calibration of the lamp and the Labsphere calibration of the diffuser. The ASD was then used to calibrate the radiance of the integrating sphere source at each of its pre-programmed illumination levels and this sphere source was used for the radiometric calibration of the ACGS. As the ACGS was operated inside a vacuum chamber, and the ASD was outside the vacuum chamber during the AGCS calibration, it was also necessary to determine the transmittance of the vacuum chamber window. The window transmittance was determined by using the ASD both inside and outside the vacuum chamber. The whole traceability chain can be seen in figure 4.

3.2. Sphere spectral output

As the radiometric calibration light source, the stability and uniformity were important characteristics of the integrating sphere and directly affected the accuracy of radiometric calibration. First, the standard deviation of the signal as measured by the interior broadband silicon detector, which was mounted so as to view the back wall of the sphere, was less than 0.3% for the duration of the tests. Second, it was important to establish the spatial homogeneity of the integrating sphere source. The ASD which has a 1° angular field of view was used to perform homogeneity scans where 37 different positions of integrating sphere exit port were recorded in a 30 mm step on an *X-Y* stage. The radiance homogeneity error defined as the relative standard deviation of the different observations was 0.65% at 0.76 μm band, 0.72% at 1.61 μm band, and 0.94% at 2.06 μm band. Third, the sphere angle radiance homogeneity was measured in a 20° conical viewing field centered in the field of view of the exit port. The results showed that the relative standard deviation of the different observations of all three bands were less than 0.5%. This result was attributed to the uniform coating of barium sulfate and the sphere baffling.

3.3. Dark current assessment

One of the most important steps in calibration was to confirm the instrument response without input radiation, which was referred to as the 'dark current response'. During operational use this dark current is subtracted from the measured signal. Since the dark current can be sensitive to the temperature of the optics and FPAs, we had to determine a way of predicting the dark current response during operation. To characterize this, the ACGS instrument was tested in the 3 m thermal vacuum chamber with no input source, with thermal variations simulating the various working modes of the payload in

orbit. The temperature variation during the thermal balance test ranged from 258 K to 180 K. High and low temperature dark response obtained during the thermal balance testing illustrated that the consistency of the dark response among channels within the same band was very good, with variations of a few digital numbers (DNs). It was also observed that the dark response in the O_2A band changed less than 3 DNs between the high and low temperatures during thermal balance testing, therefore, the dark background might be considered as constant. In contrast to the O_2A band, the weak CO_2 band and the strong CO_2 band showed a sensitivity to temperature. The two CO_2 bands dark response changed more than 100 DNs per track during thermal balance testing. Thus, a constant model of the dark response was applied for the O_2A band. For the two CO_2 bands, it was essential to discover the relationship between dark response and ambient temperature. This would be addressed in the following.

The detectors dark responses were sensitive to heat radiation. The heat radiation received by non-light-sensitive pixels was the same as for the imaging pixels. Therefore, it was possible to determine the dark background of the instrument by establishing a response relationship between the non-light-sensitive pixels and the imaging pixels. We use 16-bit binary numbers to represent the signal on the non-light-sensitive pixels in auxiliary data channel, while the data depth of imaging pixels were 14-bit binary numbers due to the restriction of FPA downlink data bandwidth. There were 12 non-light-sensitive pixels in the infrared FPA on both sides in total. During the thermal balance testing, sets of data were collected with the light source shut when no light entered the instrument over several simulated orbits. To avoid introducing errors due to noise in the algorithm, the non-light-sensitive pixels were averaged over an entire simulated orbit. We established the functional relationship between the mean of the non-light-sensitive pixels and each imaging pixel. Fortunately, this dependence was found to be well described by a simple linear function. Figure 5 shows an example of the relationship between the average of non-light-sensitive pixels and the pixel at central position of detector array. A linear fitting method was sufficient to model the dark response in each band, and the mean standard deviations of the fitting residuals were 3.98 and 3.89 respectively, indicating that this model achieved a low random error and the performance of the algorithm was very good.

These dark observations were performed under a wider variety of complex conditions than would be expected in orbit, including a wider range of instrument temperatures and voltages. During radiometric calibrations the dark current was very stable for all three spectrometers. To monitor ongoing
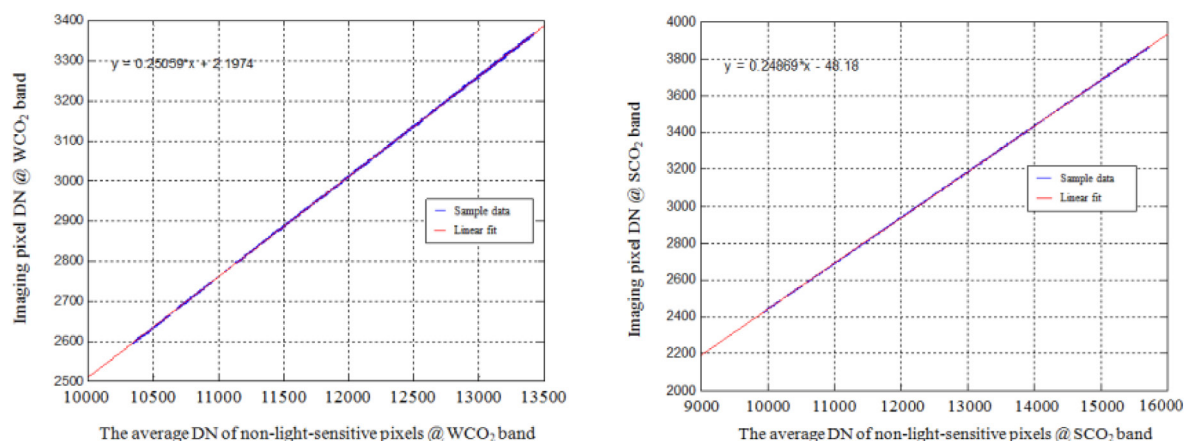
Figure 5. The relationship between the average of non-light-sensitive pixels and the pixel at central position of detector array. (Left) WCO$_2$ band. (Right) SCO$_2$ band.
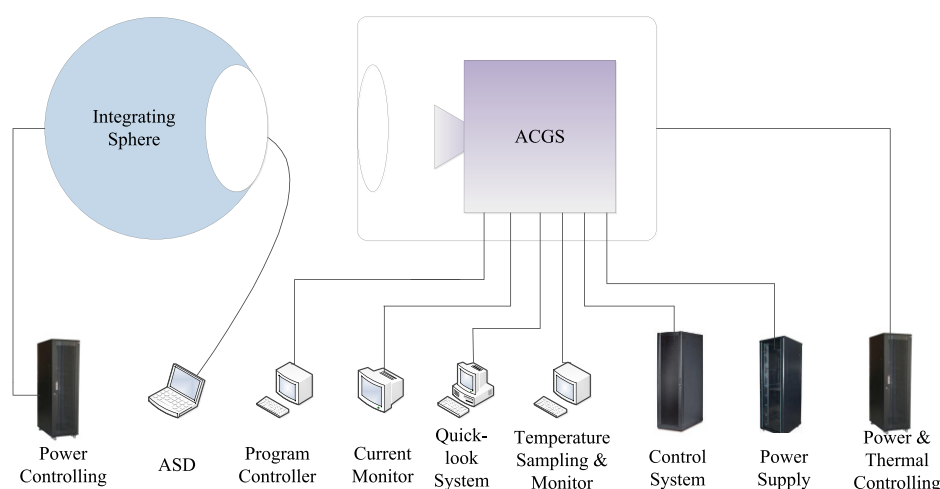

Figure 6. Radiometric calibration system of ACGS.

performance once operational, we will ensure that the dark current is measured twice in each orbit in all three bands. From these we could construct an improved dark-response model based on on-board testing data.

3.4. Radiometric gain calibration

The radiometric calibration system layout and composition are shown in figure 6, which presents all the equipment used in this paper. The 150 cm barium sulfate integrating sphere with a 20 cm exit port stayed outside the thermal vacuum chamber and the instrument was illuminated by the sphere through a fused quartz window. There were three tungsten bulbs illuminating the sphere, one was 600 W bulb inside and the other two 1000 W bulbs were outside. The baffle assembly in front of the 600 W lamp stopped light from the internal bulb reaching the ASD and ACGS directly. Each 1000 W tungsten bulb had an adjustable diaphragm. By various combinations of the bulbs and variable diaphragm, different illumination levels could be achieved. To maintain a constant temperature at the position of the assembly lamps on the sphere, a cold water circulation machine was used. The sphere was purged with dry nitrogen while in operation, which was monitored constantly by a gas

concentration monitoring meter. The ASD transfered the radiometric scale from the reference source to the ACGS instrument. The output radiance at different illumination levels of the integrating sphere was determined by the concurrent readings of the ASD and corrected for the transmittance of the window to give the radiance observed by the ACGS from within the vacuum chamber. Cubic Hermite Interpolating was used to interpolate the integrating sphere from the ASD wavelengths to the ACGS wavelengths. Through regression of the radiant intensity of the entrance aperture of the instrument against ACGS output, the radiometric gain coefficients were determined.

The purpose of the radiometric gain calibration was to determine both the radiometric gain (the conversion between DNs and radiance) and the instrument non-linearity for the ACGS. For this, the ACGS was calibrated against the integrating sphere source at different radiance levels (measured by the ASD spectrometer as described in section 3.1). The radiometric calibration should provide sufficient explanation for any nonlinearity concerning instrument gain. The response to source radiance of the instrument could be determined by gain coefficients.

The dynamic range of ACGS for the O$_2$A band was from 0.032 mW m^{-2} sr^{-1} nm^{-1} to 362.17 mW m^{-2} sr^{-1} nm^{-1}, from
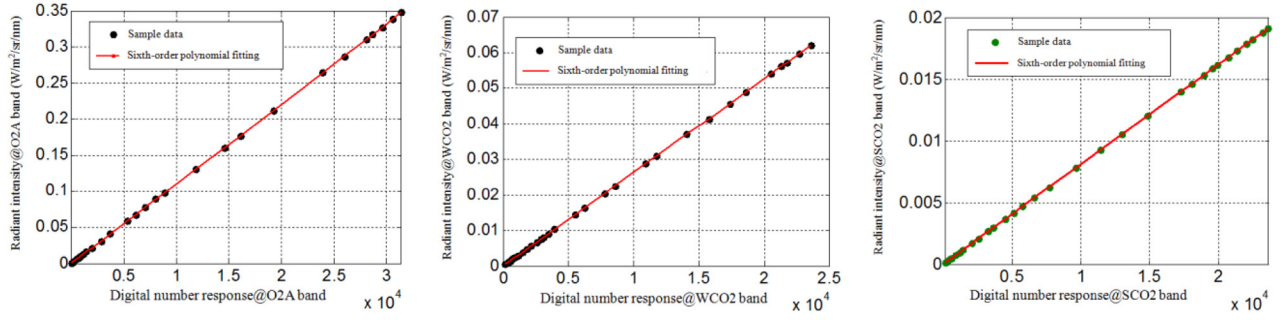
Figure 7. Radiometric response of central spectral channel in central field of view of the three bands. (Left) O_2A band. (Middle) WCO_2 band. (Right) SCO_2 band.
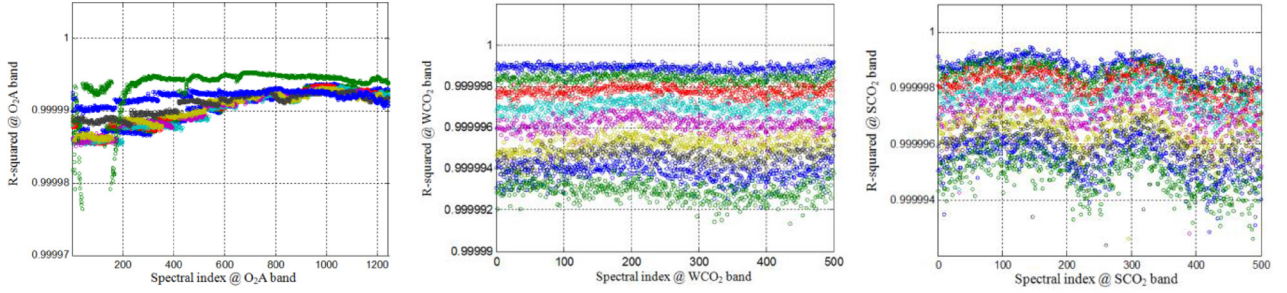

Figure 8. The statistical results of the goodness of fit. (Left) O_2A band. (Middle) WCO_2 band. (Right) SCO_2 band.

0.007 mW m^{-2} sr^{-1} nm^{-1} to 60.50 mW m^{-2} sr^{-1} nm^{-1} for the WCO_2 band, and from 0.0058 mW m^{-2} sr^{-1} nm^{-1} to 15.50 mW m^{-2} sr^{-1} nm^{-1} for the SCO_2 band. The maximum value and minimum value of the dynamic range were limited by the saturation of the detectors and random noise in signal level respectively. The typical radiance in space for the three bands were 15.2 mW m^{-2} sr^{-1} nm^{-1}, 2.6 mW m^{-2} sr^{-1} nm^{-1} and 1.1 mW m^{-2} sr^{-1} nm^{-1}. The ACGS were calibrated using various illumination levels ranging from high to low of the integrating sphere. The O_2A band was calibrated against 35 illumination levels ranging from 1.1 mW m^{-2} sr^{-1} nm^{-1} to 407.8 mW m^{-2} sr^{-1} nm^{-1}, the WCO_2 band against 34 levels from 0.5 mW m^{-2} sr^{-1} nm^{-1} to 66.0 mW m^{-2} sr^{-1} nm^{-1}, the SCO_2 band against 31 levels from 0.1 mW m^{-2} sr^{-1} nm^{-1} to 19.1 mW m^{-2} sr^{-1} nm^{-1}. We compared the results of the statistical analysis for various polynomial orders from second-order to sixth-order polynomial fittings, the sixth-order polynomial coefficients were more stable. To describe any nonlinear effects, we determined to use a sixth-order least-squares polynomial fitting, as this functional form produced lower residuals, significant at the lower end of the response range, even if the instrument response appeared to be linear-like.

$$L = k \sum_{i=0}^{6} c_i (Dn - Dn_{\text{dark}})^i. \tag{3}$$

Where L is the calibrated radiance of the integrating sphere as observed through the vacuum window by the ACGS; k is the scaling term of the gain coefficients used in flight to track the instrument changes; c_i are a set of gain coefficients derived from a fit to the polynomial equation for each spatial

footprint and each channel; Dn is the instrument readout for each sphere configuration and Dn_{dark} is the digital readout of the dark offset.

The radiometric response of central spectral channel in central field of view of the three bands is shown as figure 7. The deviation between the measured data point and the sixth polynomial fitting of the three bands was less than 2%. The statistical results of the sum of squares due to error (SSE) of fit provided an approach to describe the radiometric calibration gain coefficients. The mean values of SSE were 2.23×10^{-6} for the O_2A band, as well as 3.47×10^{-8} for the WCO_2 band, and 2.21×10^{-9} for the SCO_2 bands. The standard deviation of SSE were 1.5×10^{-8} for the O_2A band, as well as 4.91×10^{-10} for the WCO_2 band, and 8.23×10^{-11} for the SCO_2 bands. As seen in the statistical results, a sixth order polynomial fitting method fitted well to the observed data and was sufficient to model the instrument response in each band.

The goodness of fit provided another approach to describe the corresponding relationship between the regression line and real data points statistically. Figure 8 shows data of the goodness of fit calculated by sixth-order least-squares polynomial fitting with the purpose of determining the radiometric calibration gain coefficients for each channel of three bands. The R-squared values are nearly 1 in the three bands indicating that the regression line fitted the data well. In the statistical results of the goodness of fit, the standard deviations were 6.45×10^{-8} for the O_2A, 5.18×10^{-8} for the WCO_2, and 1.54×10^{-7} for the SCO_2 bands. The small standard deviations demonstrated that the radiometric calibration fitting took into account most of the variations in instrument response spanning the dynamic range of each band.

Table 3. Absolute radiometric uncertainty ($k = 1$).

Uncertainty Source	Measurement Band			Validation
	O_2A (%)	WCO_2 (%)	SCO_2 (%)	
Sphere inner surface uniformity	0.65	0.72	0.94	Measured (see section 3.2)
Sphere exit angle radiance uniformity	0.5	0.5	0.5	Measured (see section 3.2)
Sphere output stability	0.3	0.3	0.3	Measured (see section 3.2)
NIST lamp uncertainty	0.70	0.50	0.50	Vendor calibration certificate
BRDF uncertainty of diffuser	1.49	1.88	1.88	Vendor calibration certificate
Stray light	1	1	1	Estimated, not validated
ASD calibration against lamp-diffuser source	0.3	0.3	0.3	Measured (see section 3.1)
ASD output uncertainty	2	2	2	Vendor calibration certificate
ACGS radiance response uncertainty	2	2	2	Measured (see section 3.4)
Combined standard uncertainty	4.45	4.58	4.61	

3.5. Total calibration uncertainty

Table 3 shows the sources of uncertainty associated with the AGCS absolute radiometric calibration. The absolute radiometric calibration uncertainty consists of calibration source, radiometric standard transfer and response of ACGS. Error terms associated with unknown properties of calibration source include the integrating sphere inner surface uniformity, the integrating sphere exit angle radiance uniformity and the integrating sphere illumination stability. For the source of uncertainties of the radiometric standard transfer, the NIST lamp characterizing uncertainty, the BRDF uncertainty of diffuser, ASD calibration against lamp-diffuser source, stray light and the uncertainty of transfer radiometer output are contributing factors. The uncertainty of the ASD output is affected by noise, linearity, and responsivity drift with temperature. The signal-to-noise ratio of the radiometer is relatively poor when the radiance is low. Multiple measurements are used in the test to reduce the effects of random noise. Besides the uncertainty in estimating incident radiance, the instrument properties that contribute to calibration uncertainties include its SNR, dark offset, and temperature effects on the gain and offset. The following equation (4) is used to calculate the total uncertainty.

$$\sigma_{total} = \sqrt{\sigma_1{}^2 + \sigma_2{}^2 + \sigma_3{}^2 + \sigma_4{}^2 + \sigma_5{}^2 + \cdots}. \quad (4)$$

In summary, the absolute uncertainty, with a coverage factor $k = 1$, is 4.45% for the O_2A spectrometer, 4.58% for the WCO_2 spectrometer, and 4.61% for the SCO_2 spectrometer. Together, all the sources of bias and uncertainty are all well within the 5% mission requirement.

4. Bad pixels detection

Bad pixels, which degrade the image quality significantly, can not be eliminated and are due to several problems, including processing issues, technical issues and inhomogeneity in individual pixels. Although relative to the image as a whole there are only a relatively small number of bad pixels on the detector array, they can have a considerable impact on the 'summed mode' performance of the sensor. Prior to further processing, bad pixels must be identified and excluded from the 24-pixel sums, or bad pixels would contaminate the spectral samples.

The bad-pixel identification, started with the process of radiometric calibration, could be achieved by two operations. First, the instrument response data was collected in the absence of an input radiation source using full-frame mode to achieve bad-pixel identification, as dark background data reflected detector noise level of no external signals. Dark background fluctuations would affect the measurement accuracy, so bad pixels could be identified by standard deviation and average noise of the dark background. Second, several energy levels were set for the integrating sphere where the response of the detector was at the range of half-saturation and exhibited very good linearity. The pixel responsivity measured in this condition was used to detect bad pixels, as pixel responsivity data reflected detector responsiveness with an input radiation source. Therefore, the pixel responsivity fitting error could be used as another criterion for bad pixels identification.

We defined four kinds of bad pixels in the test: dead pixels, over-hot pixels, unstable pixels and over-stable pixels. We conducted the analysis of all data based on the definition that over-hot pixels and dead pixels were distinguished by

DNs reasonable range which were five times more than the mean DNs and 5 times less than the mean DNs; unstable pixels and over-stable pixels were detected by the reasonable standard deviations range which were three times more than the mean standard deviations and 3 times less than the mean standard deviations. Pixels whose responsivity was less than 1/10 of the average were taken as low responsivity pixels.

The final bad pixels included any pixel who met one or more of the following (1)–(6).

(1) The pixels which belonged to dead pixels and low responsivity pixels simultaneously; (2) The pixels which belonged to over-hot pixels and low responsivity pixels simultaneously; (3) The pixels which belonged to over-stable pixels and low responsivity pixels simultaneously; (4) In 'full-frame mode', the unstable pixels of which the maximum relative error of the fit was more than 2%; (5) The pixels whose average relative fit error of responsivity was greater than 2%; (6) The pixels whose dark background noise were eight times more than the mean standard deviations.

The number of invalid pixels was 2223 for the WCO_2 band and 2435 for the SCO_2 band, about 1.7% and 1.9% of the total number of pixels respectively. A 256-by-500 bytes array

bad-pixel map was established based on selection according to the (1) to (6) above. In the map, a value of 0 represented that a pixel was good and a value of 1 indicated that the pixel was a bad pixel which should be excluded from the spectral sample. The revised bad-pixel map could be periodically updated to the instrument after launch by solar calibration, lamp calibration and dark calibration, and could dramatically improve the quality of the spectra samples to a high degree of accuracy.

5. Conclusion

Several thermal vacuum tests were performed preflight to fully calibrate the radiometric performance of ACGS in terms of dark response and gain coefficients. Before determining other gain coefficients, the dark response and its temperature sensitivity were characterized and corrected during thermal balance test. By illuminating ACGS with the integrating sphere at more than 30 well-characterized configurations, gain coefficients were calculated for each footprint of each spectral channel among the three bands. Finally we deployed a sixth-order polynomial describing instrument's response to light. Dark background data and pixel responsivity data of full-frame mode were analyzed to identify bad pixels. A bad-pixel map was established for each CO_2 FPA base on the algorithm. The uncertainties of each band of ACGS were evaluated based on radiometric standard transfer chain, the uncertainties of the calibration source, and response of the instrument. The uncertainty analysis results showed that all the three bands had margin against the 5% absolute performance requirement.

Acknowledgments

ORCID iDs

Shuai Li ● https://orcid.org/0000-0003-4484-4945

References

[1] Basilio R R, Pollock H R and Hunyadi-Lay S L 2014 OCO-2 (orbiting carbon observatory-2) mission operations planning and initial operations experiences *Proc. SPIE* **9241** 924105

[2] Kuze A, Suto H, Shiomi K, Nakajima M and Hamazaki T 2009 On-orbit performance and level 1 data processing of TANSO-FTS and CAI on GOSAT *Proc. SPIE* **7474** 74740I

[3] Kuze A, Urabe T, Suto H, Kaneko Y and Hamazaki T 2006 The instrumentation and the BBM test results of thermal and near infrared sensor for carbon observation (TANSO) on GOSAT *Proc. SPIE* **6297** 62970K

[4] Crisp D, Miller C E and DeCola P L 2008 NASA Orbiting carbon observatory: measuring the column averaged carbon dioxide mole fraction from space *J. Appl. Remote Sens.* **2** 023508

[5] O'Brien D M, Pollock R, Polonsky I and Rogers M 2011 Identification and correction of residual image in the A-band of the orbiting carbon observatory *IEEE Trans. Geosci. Remote Sens.* **49** 2426–37

[6] Pollock R *et al* 2010 The Orbiting carbon observatory instrument: performance of the OCO instrument and plans for the OCO-2 instrument *Proc. SPIE* **7826** 78260W

[7] Zhang H, Lin C, Zheng Y, Wang W, Tian L, Liu D and Li S 2016 Development and characterization of carbon observing satellite *J. Appl. Remote Sens.* **10** 024003

[8] Zhang J, Shao J and Yan C 2014 Cloud and aerosol polarimetric imager *Proc. SPIE* **9142** 91420X

[9] Lin C, Li C, Wang L, Bi Y and Zheng Y 2014 Preflight spectral calibration of hyperspectral carbon dioxide spectrometer of TanSat *Opt. Precis. Eng.* **8** 2064–75

[10] Li Z *et al* 2017 Prelaunch spectral calibration of a carbon dioxide spectrometer *Meas. Sci. Technol.* **28** 065801

[11] Crisp D 2008 The orbiting carbon observatory: NASA's first dedicated carbon dioxide mission *Proc. SPIE* **7106** 710604

[12] Zheng Y and Gao Z 2012 Optical system design of CO_2 sounder *Opt. Precis. Eng.* **20** 2645–53

[13] Crisp D *et al* 2017 The on-orbit performance of the orbiting carbon observatory-2 (OCO-2) instrument and its radiometrically calibrated products *Atmos. Meas. Tech.* **10** 59–81

[14] O'Dell C W *et al* 2011 Preflight radiometric calibration of the orbiting carbon observatory *IEEE Trans. Geosci. Remote Sens.* **49** 2438–47

[15] Maxwell S E, Johnson B C, Rosenberg R, Chapsky L, Lee R A and Pollock R 2017 Preflight radiometric calibration of orbiting carbon observatory 2 *IEEE Trans. Geosci. Remote Sens.* **55** 1994–2006

[16] Sakuma F, Bruegge C J, Rider D, Brown D, Geier S, Kawakami S and Kuze A 2010 OCO/GOSAT preflight cross-calibration experiment *IEEE Trans. Geosci. Remote Sens.* **48** 585–99

[17] Suto H, Kawashima T, Yoshida J, Ishida J, Kuze A, Nakajima M and Hamazaki T 2008 The pre-launch performance test and calibration results of thermal and near-infrared sensor for carbon observation (TANSO) on GOSAT *Proc. SPIE* **7106** 71060L

[18] Shiomi K *et al* 2007 Calibration plan of GOSAT sensors *Proc. SPIE* **6744** 67440G